CHARACTERISATION OF ORIENTED VOLUMES IN GLACIER ICE AND EXTINCTION INVERSION WITH POL-INSAR

Jayanti J. Sharma, Irena Hajnsek, and Konstantinos P. Papathanassiou

Microwaves and Radar Institute, German Aerospace Center 82230 Wessling, Germany

ABSTRACT

In recent years there has been increased interest in using SAR to study and monitor glaciers and ice sheets for glaciological and climate change research. This paper describes the estimation of ice extinctions through the modelling of Pol-InSAR coherences as a combination of a surface contribution from the snow-ice interface and a volume response from an oriented particle cloud. Separation of the ground and volume contributions is obtained using a novel decomposition of the polarimetric covariance matrix which allows for preferential particle orientations and accounts for the influence of the dielectric constants of ice and snow. Ground-to-volume scattering ratios derived from polarimetry are used in conjunction with Pol-InSAR interferometric coherences to invert the extinction of the ice layer. Validation is performed with airborne Pol-InSAR data at L- and P-band collected using DLR's E-SAR system over the Austfonna ice cap in Svalbard, Norway as part of the ICESAR campaign.

1. INTRODUCTION

SAR is a powerful remote sensing tool with which to measure glaciers and ice sheets due to its high spatial resolution and wide coverage, and its ability to penetrate beneath the ice surface to observe sub-surface structures. However, SAR backscattering from ice remains poorly understood including the relative importance of scattering from surface and volume layers, and dependencies on frequency and glacier facie.

The objective of this paper is to isolate the volume response to enable estimation of the extinction of the ice volume. Extinction is a relevant parameter for glaciologists since it contains information on the density and internal structure of the ice. This paper describes a new technique of ice extinction estimation through the modelling of Pol-InSAR observables and coherences as a combination of contributions from a Bragg surface (at the snow-ice interface) and a volume response from an oriented particle cloud. Since ice volumes may often be expected to have a preferential orientation of scatterers, particularly horizontal stratification and layering, such an extension is important for quantitative remote sensing inversion.

The modelling approach is broken into two segments. In Section 2.1, separation of the ground and volume contributions is achieved through a novel decomposition of the polarimetric covariance matrix in which the volume is permitted to have a preferential orientation. In Section 2.2 ground-to-volume scattering ratios derived from the polarimetric decomposition are used in conjunction with Pol-InSAR interferometric coherences and an infinite, uniform-volume-under-ground model to invert ice extinctions. Experimental data collected at L- and P-band using DLR's E-SAR system are described in Section 3 and are used in Section 4 to infer extinctions of the Austfonna ice cap in Svalbard, Norway.

2. MODELLING GLACIER ICE EXTINCTIONS

2.1. Oriented volume decomposition

2.1.1. Motivation

Comparatively little research has been done to date on characterisation of the orientation properties of distributed volumetric targets using polarimetry. In [1] clouds of oriented volume particles were examined, although the coherency matrices were only modelled for scatterer orientations in the plane perpendicular to the line-of-sight (LOS), where tilt away from this plane was assumed for simplicity to be zero. In [2] sinusoidal distributions of scatterers in the plane perpendicular to the LOS were modelled.

The oriented volumes simulated in [1, 2] have the advantage of reduced complexity in the resulting covariance matrix and thus subsequent model inversion is simplified. However, the assumption that all scatterers lie exclusively in a plane perpendicular to the LOS is an oversimplification of reality from three dimensions to a two-dimensional plane. As well, results referenced to the plane perpendicular to the LOS are difficult to relate to the physical orientation of scatterers in an Earth-based coordinate system, particularly as the reference

plane changes with incidence angle. In addition, a distribution of identically-sized scatterers in the plane perpendicular to the LOS is usually assumed; however, in a volume with identically-sized particles, their projection onto the perpendicular-to-LOS plane will change their effective length as seen by the radar.

2.1.2. Oriented volume geometry

In order to model a more physically-realistic glacier ice scenario, we propose a polarimetric decomposition in which the volume of scatterers is permitted to have an orientation. In developing our model for the volumetric covariance matrix, it is assumed that topographic variations are negligible, which is reasonable for the relatively flat ice sheets examined here.

The volume is modelled as a distribution of identically-sized scatterers in three-dimensional space. For simplicity, and to reduce the number of unknowns, scatterers are assumed to be thin dipoles. We define a coordinate system with axes (x, y, z), where the z-axis is normal to the Earth's surface, x is along the line-of-flight, and y is perpendicular in a right-handed system (assuming a left-looking SAR), lying parallel to the projected ground-range direction of radar illumination. Let us further write (x, y, z) in a spherical coordinate system defined by angles (ω, ψ) and radius r such that:

$$\begin{bmatrix} x \\ y \\ z \end{bmatrix} = r \begin{bmatrix} \cos\omega\cos\psi \\ \sin\omega\cos\psi \\ \sin\psi \end{bmatrix}, \qquad (1)$$

where $-\pi/2 \leq \psi \leq \pi/2$ and $0 \leq \omega \leq 2\pi$, illustrated in Fig.1. The radar geometry is defined by a new coordinate system (x', y', z') created by a rotation about the x-axis by $-\tau_0$, where τ_0 is the complement of the incidence angle ($\tau_0 = \pi/2 - \theta_{\text{inc}}$). Line-of-sight is along the y'-axis and the plane perpendicular to the LOS can be defined by the $x'z'$-plane. The horizontal polarisation H-axis is along the line-of-flight, and the vertical polarisation V-axis is perpendicular to the $x'y'$-plane. The relation between the radar geometry and the (ω, ψ) coordinate system is shown in Fig.1. The relation between (x, y, z) and (x', y', z') is then:

$$\begin{bmatrix} x' \\ y' \\ z' \end{bmatrix} = \begin{bmatrix} 1 & 0 & 0 \\ 0 & \cos(-\tau_0) & \sin(-\tau_0) \\ 0 & -\sin(-\tau_0) & \cos(-\tau_0) \end{bmatrix} \begin{bmatrix} x \\ y \\ z \end{bmatrix}$$

$$= r \begin{bmatrix} \cos\omega\cos\psi \\ \sin\omega\cos\psi\cos\tau_0 - \sin\psi\sin\tau_0 \\ \sin\omega\cos\psi\sin\tau_0 + \sin\psi\cos\tau_0 \end{bmatrix}. \qquad (2)$$

2.1.3. Oriented volume covariance matrix

Considering a single dipole, the equivalent scattering matrix observed by a monostatic radar for this particle can be expressed as a function of ω, ψ and τ_0 given its projection onto the H (i.e. x') and V (i.e. z') axes from Eq. 2.
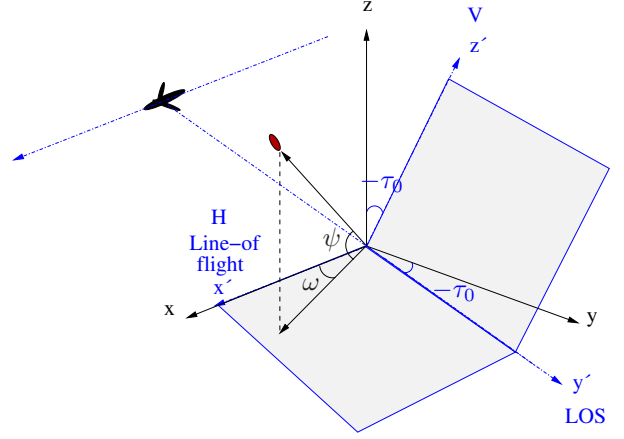

Figure 1: Relation between Earth-based (x, y, z) and radar geometry (x', y', z') coordinate systems. Orientation of a single particle (in red) is shown, described by orientation angles (ω, ψ).

It is assumed that the distance between the sensor and the volume of particles is very large, such that as seen from the radar r (Eq. 2) can be considered constant for all particles. The scattering matrix is then:

$$[\boldsymbol{S}_{\text{dipole}}](\omega, \psi, \tau_0) = \begin{bmatrix} S_{HH} & S_{HV} \\ S_{VH} & S_{VV} \end{bmatrix} \qquad (3)$$

where

$$S_{HH} = \cos^2(\psi)\cos^2(\omega)$$
$$S_{VV} = (\sin\omega\cos\psi\sin\tau_0 + \sin\psi\cos\tau_0)^2$$
$$S_{HV} = S_{VH}$$
$$\quad = \cos\psi\cos\omega(\sin\omega\cos\psi\sin\tau_0 + \sin\psi\cos\tau_0).$$

Except for a complex reflectivity scaling factor, the backscattering response from a single deterministic particle is completely described by $[\boldsymbol{S}]$ in Eq. 3. To determine the superposition of responses from a distribution of particles within a volume for the monostatic case, the covariance matrix is given by:

$$[\boldsymbol{C}] = \begin{bmatrix} \langle|S_{HH}|^2\rangle & \sqrt{2}\langle S_{HH}S_{HV}^*\rangle & \langle S_{HH}S_{VV}^*\rangle \\ \sqrt{2}\langle S_{HV}S_{HH}^*\rangle & 2\langle|S_{HV}|^2\rangle & \sqrt{2}\langle S_{HV}S_{VV}^*\rangle \\ \langle S_{VV}S_{HH}^*\rangle & \sqrt{2}\langle S_{VV}S_{HV}^*\rangle & \langle|S_{VV}|^2\rangle \end{bmatrix},$$

$$(4)$$

where $*$ denotes the complex conjugate and $\langle\ldots\rangle$ represents the ensemble average.

In summing the responses from a distribution of particles, it is assumed that only single scattering is significant and that the scatter from each particle in the cloud is independent of its neighbours [1]. Assuming ω and ψ to be independent variables with probability density functions $p(\omega)$ and $p(\psi)$, respectively, the expected value for each element mn in the volume covariance matrix can be determined through integration of the pdfs over all possible orientation angles and for each linear polarisation combi-

nation ij:

$$\langle C_{v\,mn}\rangle = \int_0^{2\pi}\int_{-\pi/2}^{\pi/2} S_i S_j^* \,|\cos\psi|\,p(\psi)p(\omega)\,d\psi\,d\omega, \quad (5)$$

where the $|\cos\psi|$ term is required for equal weighting on the unit circle for each incremental surface area $d\psi \times d\omega$. Differential phase due to propagation of the signal through an oriented volume is not accounted for in Eq. 5.

Various distribution functions $p(\psi)$ and $p(\omega)$ are possible. Results from simulations in which ψ is fixed to 0 and ω is modelled as a uniform distribution centred at ω_0 with width $2\Delta\omega$ are given in Fig.2. Probability density function $p(\omega)$ is thus:

$$p(\omega) = \begin{cases} \frac{1}{2\Delta\omega} & \text{for } \omega_0 - \Delta\omega \le \omega \le \omega_0 + \Delta\omega \\ 0 & \text{otherwise.} \end{cases} \quad (6)$$

To obtain Fig.2, the integrals from Eq. 5 were evaluated and $[\boldsymbol{C_v}]$ components were determined as a function of $\Delta\omega$ for $\omega_0 = 0°$. Results are plotted for both nadir ($\theta = 0°$) and an incidence angle of $40°$. Results at $\theta = 0°$ are identical to those using the conventional 2-D model given in e.g. [1]. However, as incidence angle is increased, it is seen that backscatter at VV and HV differ significantly from that predicted assuming scatterers lie in the perpendicular-to-LOS plane. For this reason a 3-D model is required for accurate modelling.
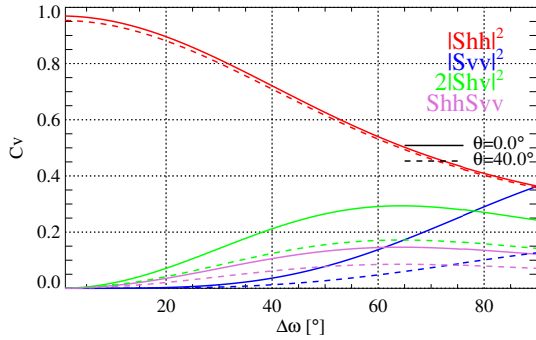

Figure 2: Normalised covariance matrix components for simulations of an oriented volume versus distribution widths for $\omega_0 = 0°$, and fixed $\psi = 0°$. Results at both nadir (solid) and $\theta_{\text{inc}} = 40°$ (dashed) are given.

As mentioned above, many possibilities exist in choosing $p(\psi)$ and $p(\omega)$. To minimise the number of unknowns we assume a random distribution of scatterers in either ψ or ω, and a uniform distribution over a finite width for the other. Simulations carried out show that modelling a random distribution in ψ and an oriented ω rather than the opposite allows more sensitivity to a varying width parameter $\Delta\omega$, and is better able to reconstruct the large HH/VV backscatter ratios seen in our experimental data of glacier ice. This modelling scenario is equivalent to assuming preferential orientation in the plane parallel to the Earth's surface and a completely random distribution in the direction normal to the Earth's surface.

We assume a completely random distribution of ψ such that $p(\psi) = 1/\pi$. In ω, the volume is modelled as a uniform distribution of identically-sized scatterers as given by Eq. 6. Other probability density functions, such as a Gaussian distribution, are also possible, although are more mathematically involved.

Integrating Eq. 5 over ψ and ω for all linear polarisation combinations ij, the following volume covariance matrix is obtained:

$$[\boldsymbol{C_v}] = \frac{f_v}{\Delta\omega} \begin{bmatrix} f_{11} & f_{12} & f_{13} \\ f_{12} & 2f_{13} & f_{23} \\ f_{13} & f_{23} & f_{33} \end{bmatrix} \quad (7)$$

where

$$f_{11} = 12\Delta\omega + 8\cos(2\omega_0)\sin(2\Delta\omega) + \cos(4\omega_0)\sin(4\Delta\omega)$$

$$f_{12} = -4\sqrt{2}(\cos^4(\Delta\omega - \omega_0) - \cos^4(\Delta\omega + \omega_0))\sin(\tau_0)$$

$$f_{13} = 4\Delta\omega + 2\cos^2(\tau_0)\cos(2\omega_0)\sin(2\Delta\omega)$$
$$- \cos(4\omega_0)\sin(4\Delta\omega)\sin^2(\tau_0)$$

$$f_{23} = \frac{1}{\sqrt{2}}(-\sin(2\Delta\omega)(9\sin(\tau_0) + \sin(3\tau_0))\sin(2\omega_0)$$
$$+ 2\sin(4\Delta\omega)\sin(\tau_0)^3\sin(4\omega_0))$$

$$f_{33} = 12\Delta\omega - 2(5 + \cos(2\tau_0))\cos(2\omega_0)\sin(2\Delta\omega)\sin^2(\tau_0)$$
$$+ \cos(4\omega_0)\sin(4\Delta\omega)\sin^4(\tau_0)\,,$$

where f_v is a scaling factor. Note that the $[\boldsymbol{C_v}]$ matrix is now fully populated, although for $\omega_0 = 0°$ or $\omega_0 = 90°$, the cross-terms representing co- and cross-pol correlation (e.g. $\langle S_{HH}S_{HV}^*\rangle$ and $\langle S_{HV}S_{VV}^*\rangle$ terms from Eq. 4) disappear.

The variation of $[\boldsymbol{C_v}]$ components with varying width $\Delta\omega$ for $\omega_0 = 0°$ and random ψ at a fixed incidence angle of $\theta_{\text{inc}} = 40°$ are given in Fig.3. It is seen that the model pre-
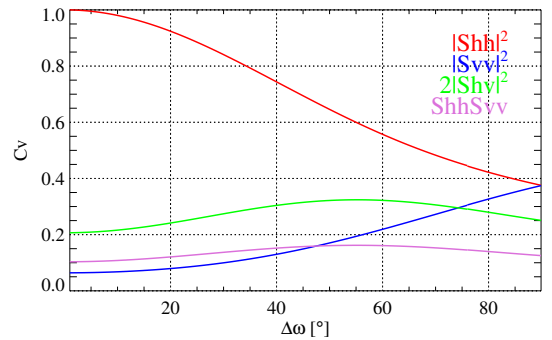

Figure 3: Normalised covariance matrix components for simulations of an oriented volume versus distribution widths for $\theta_{\text{inc}} = 40°$, $\omega_0 = 0°$, and random ψ.

dicts larger HH than VV except at $\Delta\omega=90°$ which represents completely random scattering. Variation in $\Delta\omega$ can be used to model a wide range of HH/VV polarisation ratios, which is necessary to reconstruct the polarimetric properties seen in the experimental data.

2.1.4. Polarimetric decompositions with dielectric media

Transmissivities can also be integrated into the above model, as is required for dielectric media such as ice and snow. In this study, the dielectric constant ε_r was computed from an empirical relation to firn density [3], where firn is defined as dense snow which has survived at least one summer. An approximate firn density of $\rho_{\text{firn}} = 0.8$ g/cm^3 (the mean of a 16 m ice core extracted near the test area) yielded relative permittivity $\varepsilon_{\text{firn}} = 2.8$ and assuming a snow density of 0.4 g/cm^3 gives $\varepsilon_{\text{snow}} = 1.7$.

Negligible reflection at the air-snow boundary [4] and no scattering within the snowpack are assumed, which are reasonable for dry-snow at L- and P-band wavelengths. At the snow-firn interface it is assumed that the surface is relatively smooth with respect to the wavelength and transmissitivities are approximated using the Fresnel equations [5]. In reality the transmissitivities will be lower since surface roughness will create additional scattering. However, this additional scattering factor, assumed to be polarisation-independent, will be absorbed into the f_v factor in $[C_v]$, and the transmissitivities principal influence here is to account for differences in transmission coefficients between polarisations, which becomes more pronounced with increasing incidence angle. The angle of refraction in the volume θ_r is determined from successive application of Snell's law to a signal propagating through the air-snow and snow-ice interfaces. τ_0 in Eq. 7 is now given as $\tau_0 = \pi/2 - \theta_r$.

Two-way transmissivities are represented as Υ_s (for horizontal polarisation) and Υ_p (for vertical polarisation), derived from knowledge of the dielectric constants and θ_r. Accounting for transmission yields a slightly modified version of the volume covariance matrix from Eq. 7, where $C_{v\,mn}$ represents the corresponding component from Eq. 7:

$$[C_v(\Upsilon)] = \frac{f_v}{\Delta\omega} \begin{bmatrix} \Upsilon_s^2 C_{v11} & 0 & \Upsilon_s\Upsilon_p C_{v13} \\ 0 & \Upsilon_s\Upsilon_p C_{v22} & 0 \\ \Upsilon_s\Upsilon_p C_{v31} & 0 & \Upsilon_p^2 C_{v33} \end{bmatrix},$$ (8)

where a centre of distribution of $\omega_0 = 0°$ or $90°$ was assumed such that terms with co-/cross correlations reduce to 0.

2.1.5. Oriented volume and surface decomposition

Applying the results from the previous section, a polarimetric decomposition consisting of a Bragg surface (described by the Small Perturbation Model or SPM) overlying an oriented volume is proposed. The surface covariance matrix $[C_s]$ is similar to that modelled by the Freeman 3-component distribution in [6], although we fix β to conform to the SPM using knowledge of the approximate snow and ice dielectric constants:

$$[C_s] = f_s \begin{bmatrix} |\beta|^2 & 0 & \beta \\ 0 & 0 & 0 \\ \beta^* & 0 & 1 \end{bmatrix}$$ (9)

where

$$\beta = \frac{R_s}{R_p} e^{j(\phi_h - \phi_v)}$$ (10)

$$f_s = m_s^2 |R_p|^2.$$ (11)

In Eqs. 10 and 11 R_s and R_p are the Bragg coefficients for horizontally and vertically polarised waves [4], ϕ_h and ϕ_v are the horizontal and vertical phase components and m_s is a function of the wavenumber and surface roughness parameters. R_s and R_p are fixed using the equations from [4]. As the source of a β phase is not well established, we model only $|\beta|^2$.

Assuming surface and volume scatter components are uncorrelated, the combined covariance matrix is a sum of the matrices for the individual mechanisms [6]. From Eqs. 8 and 9 the model for the combined covariance matrix is thus:

$$[C_{\text{total}}] = [C_s] + [C_v(\Upsilon)]$$ (12)

where subscript s is surface and v is volume, and reflection symmetry has been assumed such that like- and cross-polarised returns are uncorrelated. The system of equations consists of 3 radar observables (three magnitudes $|S_{hh}|^2$, $|S_{vv}|^2$, $|S_{hv}|^2$) and 4 unknowns: f_s, f_v, $\Delta\omega$ and ω_0. Fixing ω_0 to $0°$ or $90°$, the number of unknowns is reduced to 3 such that the system of equations is invertible.

The centre orientation angle ω_0 is determined by comparing modelled $|\beta|^2$ to the observed polarisation ratio $|S_{hh}|^2/|S_{vv}|^2$ with the following decision rule:

$$\omega_0 = \begin{cases} 0° & \text{for} \quad \frac{|S_{hh}|^2}{|S_{vv}|^2} > |\beta|^2 \\ 90° & \text{for} \quad \frac{|S_{hh}|^2}{|S_{vv}|^2} \leq |\beta|^2 \end{cases}$$ (13)

where $\omega_0 = 0°$ corresponds to scatterers oriented parallel to the line-of-flight, and $\omega_0 = 90°$ corresponds to scatterers oriented perpendicular to the line-of-flight, and it is assumed that scatterers have randomly distributed vertical orientation angles ψ. Eqn. 12 is solved numerically; the solution is constrained to physically-realistic scenarios by requiring $f_s \geq 0$, $f_v \geq 0$ and $0 < \Delta\omega \leq \pi/2$.

2.2. Extinction estimation using Pol-InSAR

In the previous section polarimetric decomposition was used to separate contributions from surface and volume

scattering mechanisms for each linear polarisation. In order to use this information to compute extinction values, we define m, the ground-to-volume scattering ratio, to quantify the relative surface and volume contributions. Vector $\boldsymbol{m} = [m_{\mathrm{HH}}, m_{\mathrm{HV}}, m_{\mathrm{VV}}]$ is computed using the powers along the main diagonals of the modelled covariance matrices as follows:

$$
\begin{bmatrix} m_{\mathrm{HH}} \\ m_{\mathrm{HV}} \\ m_{\mathrm{VV}} \end{bmatrix} = \begin{bmatrix} \frac{C_{s\,11}}{C_{v\,11}(\Upsilon)} \\ \frac{C_{s\,22}}{C_{v\,22}(\Upsilon)} \\ \frac{C_{s\,33}}{C_{v\,33}(\Upsilon)} \end{bmatrix} = \begin{bmatrix} \frac{C_{s\,11}}{C_{v\,11}(\Upsilon)} \\ 0 \\ \frac{C_{s\,33}}{C_{v\,33}(\Upsilon)} \end{bmatrix}. \quad (14)
$$

Note that $m_{\mathrm{HV}} = 0$ because the decomposition model assumes the surface power contributed by the C_{s22} element in Eq. 9 to be zero.

The ground-to-volume scattering ratios are then used in combination with Pol-InSAR interferometric coherences and an infinite-uniform-volume-under-ground model for determination of the ice extinction coefficient. The extinction κ_e accounts for the combined effect of absorption and scattering in the medium and may be expressed in terms of the penetration depth d_{pen} at which the one-way backscattered power falls to $1/e$ given by [4]:

$$
\kappa_e = -\cos\theta_r / d_{\mathrm{pen}}, \quad (15)
$$

where the $\cos\theta_r$ factor accounts for the off-vertical travel distance of the wave within the medium. κ_e is the extinction coefficient in units of Nepers m^{-1}, although it is conventionally quoted in decibels as $\sim 8.686 \cdot \kappa_e$ dB/m.

Let γ_z represent the coherence from a combination of volume scattering with complex coherence γ_{vol} and a surface scattering component at the snow-ice interface whose strength is determined by the positive scalar m. After correction of SNR and range spectral decorrelation the coherence magnitude is given as [7]:

$$
|\gamma_z| = \left| \frac{\gamma_{\mathrm{vol}}(\kappa_e) + m}{1 + m} \right|, \quad (16)
$$

where, assuming an infinite, uniform volume γ_{vol} can be represented by:

$$
\gamma_{\mathrm{vol}} = \frac{1}{1 + \frac{j\cos\theta_r k_{z\mathrm{vol}}}{2\kappa_e}}. \quad (17)
$$

In Eq. 17 j is the imaginary number and $k_{z\mathrm{vol}} = \frac{4\pi\sqrt{\varepsilon}}{\lambda} \frac{\Delta\theta_r}{\sin\theta_r}$ is the vertical wave number in the volume; λ is the wavelength in free space, ε_r the ice permittivity and $\Delta\theta_r$ the difference in look angles from each antenna in the volume.

With knowledge of $\boldsymbol{m}$ from Eq. 14, κ_e can be determined using Eqs. 16 and 17 at each polarisation and each pixel independently:

$$
\kappa_e = \frac{\cos(\theta_r)|k_{z\,\mathrm{vol}}|}{2(1+m)} \sqrt{\frac{m^2 - |\gamma_z|^2(1+m)^2}{|\gamma_z|^2 - 1}}, \quad (18)
$$

where m, $|\gamma_z|$ and κ_e are polarisation-dependent.

3. EXPERIMENTAL DATA

The test site lies near the summit of the Austfonna ice cap on the island of Nordaustlandet in northeastern Svalbard, Norway ($\sim$80°N, 25°E) in the subpolar glacial regime. The model from Section 2 is applied to a unique Pol-InSAR data set acquired over the Nordaustlandet ice sheet. The SAR data were collected using DLR's airborne E-SAR (Experimental SAR) system as part of the ICESAR campaign in March and April 2007. Repeat-pass fully-polarised multi-baseline data at L- (1.3 GHz) and P-band (0.35 GHz) frequencies were obtained. The along-track direction was oriented approximately parallel to the glacier centre line, which corresponds to the steepest gradient and predominant flow direction.

4. RESULTS AND DISCUSSION

4.1. Oriented volume decomposition model applied to experimental data

The oriented volume decomposition from Section 2.1.5 was applied on a pixel-by-pixel basis to the experimental data. Illustrations of each component for L- and P-band are given in Figs. 4 and 5, respectively. The L- and P-band data are not coregistered, but represent approximately the same area. For pixels coloured white no acceptable fit to the model could be found.

Both L- and P-band exhibit decreased surface power with increasing incidence angle as expected from scattering theory. At L-band the scene is very homogeneous and few ice features are discernible. At P-band more ice structure is visible, with increased volume scatter P_v in an irregularly-shaped area in the upper-left and along a ridge-type feature in far-range. The test site lies in the percolation zone and these regions could correspond to areas of enhanced melt features such as ice pipes and lenses.

Flight lines run parallel to the approximate ice flow direction, such that channels created from drainage and spring run-off should run parallel to the line-of-flight and if discernible in the radar imagery, should have a narrow distribution about $\omega_0 \simeq 0°$. Prevailing winds are also in the along-track direction, potentially forming sastrugi (snow dunes) typically a metre to several metres in size also aligned in the downwind direction [8].

For L-band in Fig.4 (c), it is seen that the majority of pixels fulfill conditions for $\omega_0 \simeq 0°$, determined using Eq. 13. L-band HH backscatter is greater than VV for all incidence angles, which the model attributes to the presence of scatterers oriented along the H-axis. The orientation widths are fairly large, increasing from $\sim$70° in near-range to nearly 90°, i.e. a random volume, in mid-range. In far-range there is greater variation with $\Delta\omega \sim 50 - 90°$. The slightly narrower near-range widths are likely due to near-range crevassing, visible in Pauli

images of the data. In far-range those pixels with narrow $\Delta\omega$ correlate well with pixels possessing large HH/VV polarisation ratios, although no individual ice features can be made out.

For P-band HH and VV backscatter are more similar, with many pixels exhibiting random volume type behaviour ($\Delta\omega \simeq 90°$ in Fig.5 (d)), especially in the areas of suspected percolation features earlier identified as having increased volume scatter. However, throughout a large swath in mid-range, $\omega_0 = 0°$ and orientation widths are significantly narrower with $\Delta\omega \simeq 40°$. In these areas VV backscatter is low in comparison with HH, which is attributed to a strong orientation of scatterers parallel to the H-axis, possibly due to buried drainge channels (used to transport summer melt downglacier) and to sastrugi and buried sastrugi. P-band is likely more sensitive than L-band to these features because volume scattering from small, randomly-oriented ice crystals is reduced at the longer wavelength.
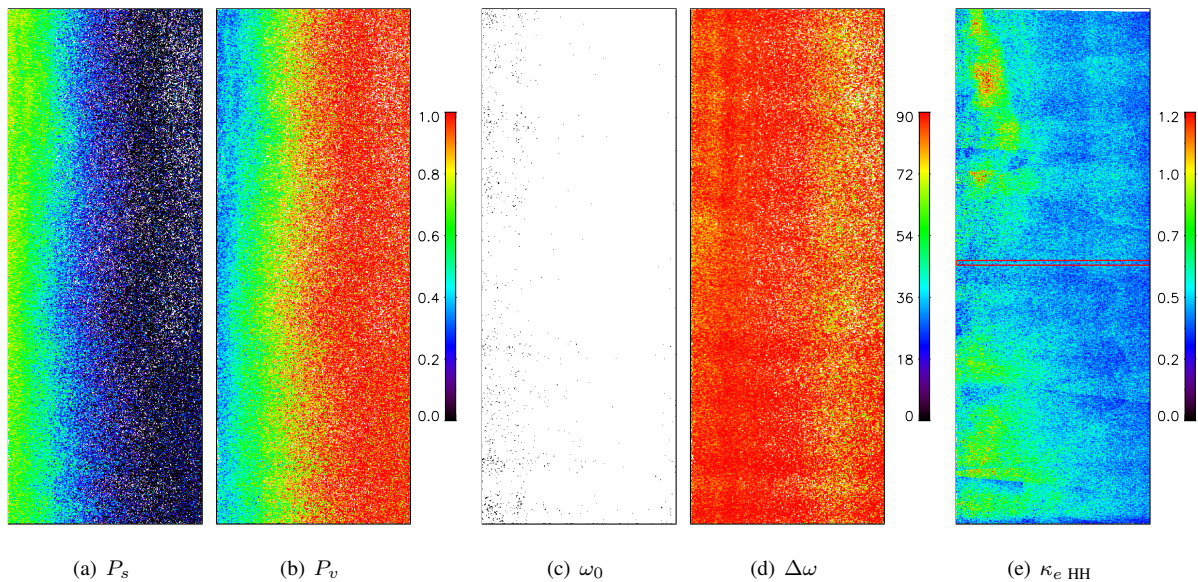

(a) P_s (b) P_v (c) ω_0 (d) $\Delta\omega$ (e) $\kappa_{e\,HH}$

Figure 4: Oriented volume and surface SPM decomposition for L-band. P_s, P_v, ω_0 and $\Delta\omega$ represent the normalised surface power, normalised volumetric power, orientation distribution centre (white: ω_0= 0°, black: ω_0= 90°) and orientation distribution width, respectively. Extinctions κ_e [dB/m] are shown for HH in (e). Flight (azimuth) direction is from top to bottom, range direction from left to right.
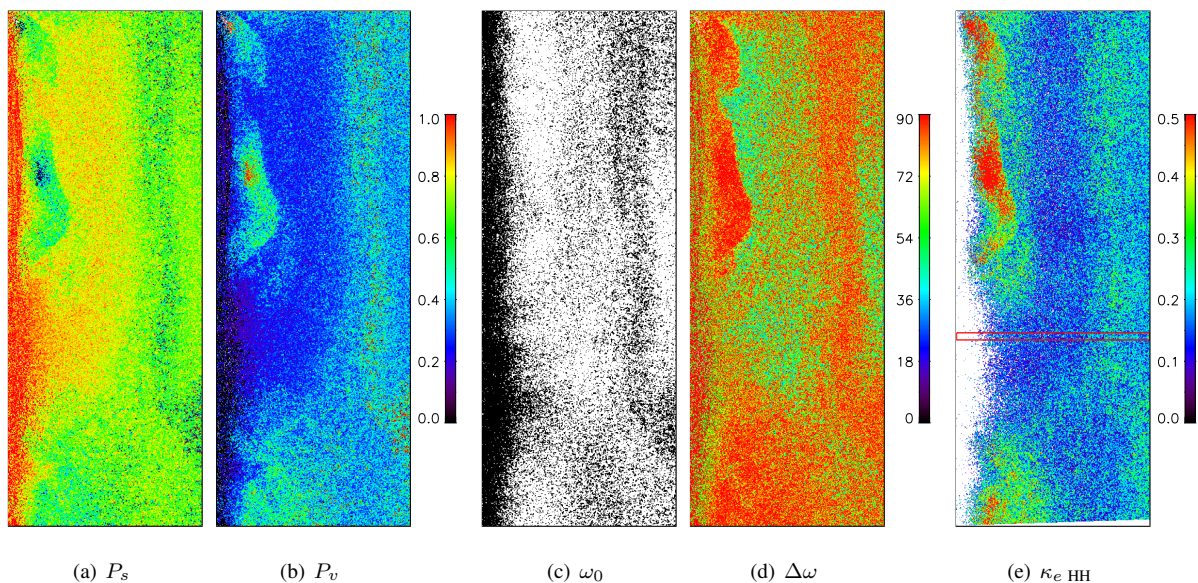

(a) P_s (b) P_v (c) ω_0 (d) $\Delta\omega$ (e) $\kappa_{e\,HH}$

Figure 5: Oriented volume and surface SPM decomposition for P-band. Extinctions κ_e [dB/m] are shown for HH in (e).

## 4.2. Extinction inversion applied to experimental data

Ratios of the volume and scattering components from Section 4.1 yield estimated ground-to-volume scattering ratios, which are then used in conjunction with Eq. 17 for extinction estimation at each polarisation. Extinction results from multiple baselines are combined by first applying a mask of $0.01 < k_z < 0.1$ to eliminate solutions from extremely small baselines (which have virtually no interferometric sensitivity) and from longer baselines more susceptible to insufficiencies in modelling and to small errors in m. Results are then averaged from the remaining valid baselines on a pixel-by-pixel basis. Results across the entire scene at HH for L- and P-band are shown in Fig.4 (e) and Fig.5 (e), where pixels coloured white could not be inverted. Such pixels generally occur when the square root in Eq. 18 becomes negative due to a large m which is inconsistent with the measured decorrelation $|\gamma_z|$.

To examine trends with incidence angle for all polarisations, extinctions for a subset (50 azimuth pixels wide) averaged through azimuth and smoothed in range for a relatively homogeneous area are shown in Fig.6. The locations of these subsets are shown in red in Fig.4 (e) and Fig.5 (e). For ease of comparison subset boxes were chosen at roughly the same location for L- and P-band.

Examining results at HH over the entire scene, extinctions are fairly homogeneous at L- and P-band, with background values of ~ 0.4 dB/m and 0.2 dB/m, respectively, and with clearly defined areas of high extinctions corresponding to potential percolation features such as ice lenses and ice pipes. At P-band near-range values could not be inverted, likely due to overestimated ground-to-volume ratios m which result in a negative square root in Eq. 18. In near-range effective baselines are larger and thus model sensitivity is greater, such that even small errors in m or noise in the coherence can have a large impact on extinction estimation.

The subsets in Fig.6 display extinction results for all polarisations. At L-band the extinctions for the co-pol polarisations HH and VV are approximately equal in mid- to far-range. The oriented-behaviour observed in far-range in Fig.4 (d) does not manifest itself as a strong differential κ_e between co-pols, since surface scattering and thus m are very low for both HH and VV in far-range, and thus have minimal impact upon extinction inversion.

In the polarimetric decompositions in Section 4.1 P-band was characterised by narrower orientation distributions than L-band, and thus we would expect to see increased differential extinctions between polarisations at this frequency, and higher HH than VV extinctions across much of the swath where $\omega_0 \simeq 0°$. This agrees well with Fig.6 (b), where $\kappa_{e\,HH} > \kappa_{e\,VV}$ from $30° \leq \theta_{inc} \leq 45°$. At $\theta_{inc} \simeq 47°$ the effects of the random volume type ridge feature are seen and, as expected, extinctions at all polarisations are roughly equal. In near-range conclusions are difficult to make as very few HH pixels could be inverted
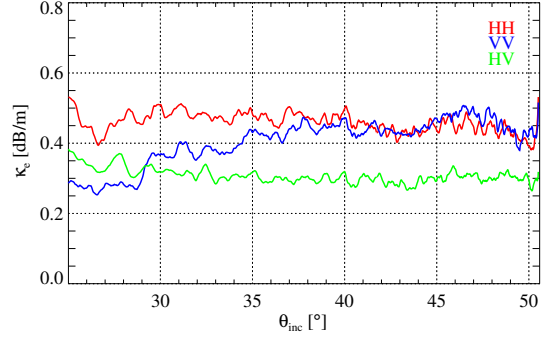
(a) L-band Extinctions
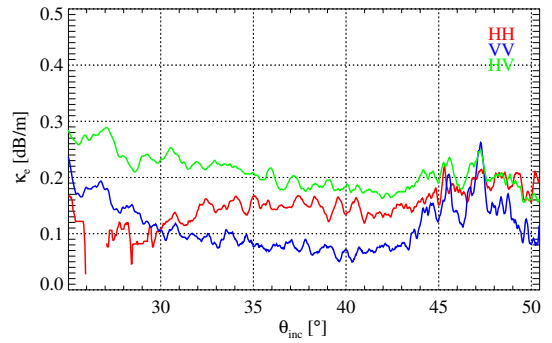
(b) P-band Extinctions

Figure 6: Extinction (κ_e) versus incidence angle (θ) for subsets from Figs. 4 and 5.

and thus results are quite noisy.

Although extinctions have been successfully inverted, there remain unresolved issues. In [9] it was shown that extinctions inverted at large effective baselines are more sensitive to any unmodelled ground contributions. In addition, larger baselines result in lower and thus noisier coherence magnitudes, contributing additional uncertainties to extinctions inverted for smaller incidence angles. The Small Perturbation Model used in this study for surface modelling predicts an HV surface backscatter contribution of zero and in some instances, especially at P-band, $\kappa_{e\,HV}$ is larger than co-pol extinctions and shows a decreasing trend with incidence angle, indicating that perhaps the assumption of $m_{HV} = 0$ is inappropriate. A relatively simple scattering model was implemented including such assumptions as dipole-shaped volume scatterers, a random distribution in vertical angle ψ and an infinite, uniform-volume-under-ground scenario. A more complete and accurate characterisation of glacier ice would require more sophisticated EM models addressing such effects as resonance and multiple scattering, although such models often lead to underestimated inversion problems due to an increased number of parameters.

5. SUMMARY

In this paper orientations of particles in glacier ice are characterised and extinctions inverted after the removal of a surface scattering component from the interferometric coherence. Separation of the ground and volume contributions is obtained through a novel decomposition of the polarimetric covariance matrix in which the volume is permitted to have a preferential orientation. The proposed model has the advantage of a direct relation of the angles ω and ψ to an Earth-based reference system, aiding in physical interpretation. Additionally it allows for a full three-dimensional distribution of volume particles not constrained to the plane perpendicular to the LOS. Polarimetric-dependent transmission coefficients of the signal into the ice volume were also integrated into the decomposition.

Extra HH scattering observed in the experimental data is proposed to originate from scatterers oriented parallel to the line-of-flight which coincides with the glacier centre line, along which dendritic drainage features and buried sastrugi could likely be oriented. Without ground surveys and data collected at different azimuth aspect angles however, this hypothesis cannot be confirmed.

Estimation of glacier volume parameters using longer-wavelength Pol-InSAR observables is important for future spaceborne concepts. Potential satellite missions including the BIOMASS Earth observation proposal would benefit from an increased understanding of SAR observables over glacier ice. The extinctions inverted from the experimental data over Austfonna at L- and P-band could be used in identifying areas of melt features and other ice inclusions. As well, additional information may be available using the orientation parameters derived at the decomposition stage. Future work will concentrate on interpretation of these features and on a validation of extinctions using ground penetrating radar measurements.

ACKNOWLEDGMENTS

REFERENCES

[1] S. R. Cloude, J. Fortuny, J. Lopez-Sanchez, and A. Sieber, "Wide-band polarimetric radar inversion studies for vegetation layers," *IEEE Trans. Geosci. Remote Sens.*, vol. 37, no. 5, pp. 2430–2441, September 1999.

[2] Y. Yamaguchi, T. Moriyama, M. Ishido, and H. Yamada, "Four-component scattering model for polarimetric SAR image decomposition," *IEEE Trans. Geosci. Remote Sens.*, vol. 43, no. 8, pp. 1699–1706, August 2005.

[3] C. Mätzler, "Applications of the interaction of microwaves with natural snow cover," *Remote sensing reviews*, vol. 2, pp. 259–387, 1987.

[4] F. Ulaby, R. Moore, and A. Fung, *Microwave Remote Sensing, Active and Passive, Volume II: Radar Remote Sensing and Surface Scattering and Emission Theory*. Norwood, MA: Addison-Wesley, 1982.

[5] F. T. Ulaby, R. K. Moore, and A. K. Fung, *Microwave Remote Sensing, Active and Passive, Volume I: Fundamentals and Radiometry*. Norwood, MA: Addison-Wesley, 1981.

[6] A. Freeman and S. L. Durden, "A three-component scattering model for polarimetric SAR data," *IEEE Trans. Geosci. Remote Sens.*, vol. 36, no. 3, pp. 963–973, May 1998.

[7] J. J. Sharma, I. Hajnsek, and K. P. Papathanassiou, "Multi-frequency Pol-InSAR signatures of a subpolar glacier," in *3rd Intl. Workshop on Sci. and Appl. of SAR Polarimetry and Polarimetric Interferometry (PolInSAR2007)*, Frascati, Italy, 22-26 January 2007.

[8] R. Bindschadler, "Tracking subpixel-scale sastrugi with Advanced Land Imager," *IEEE Trans. Geosci. Remote Sens.*, vol. 41, no. 6, pp. 1373–1377, June 2003.

[9] J. J. Sharma, I. Hajnsek, and K. P. Papathanassiou, "Extinction estimation over land ice using long-wavelength polinsar," in *Proc. of the European Conference on Synthetic Aperture Radar (EUSAR)*, vol. 1, Friedrichshafen, Germany, 02-05 June 2008, pp. 201–204.